



# Microstructures, tensile properties and serrated flow of $\text{Al}_x\text{CrMnFeCoNi}$ high entropy alloys

Jun XU, Cheng-ming CAO, Ping GU, Liang-ming PENG

CAS Key Laboratory of Mechanical Behavior and Design of Materials,  
Department of Modern Mechanics, School of Engineering Science,  
University of Science and Technology of China, Hefei 230027, China

Received 21 June 2019; accepted 30 December 2019

**Abstract:** Microstructures and mechanical properties of dual-phase  $\text{Al}_x\text{CrMnFeCoNi}$  ( $x=0.4, 0.5, 0.6$ , at.%) alloys were investigated. Thermomechanical processing leads to a microstructural evolution from cast dendritic structures to equiaxed ones, consisting of face-centered cubic (fcc) and body-centered cubic (bcc) phases in the two states. The volume fraction of bcc phase increases and the size of fcc grain decreases with increasing Al content, resulting in remarkably improved tensile strength. Specifically, the serrated flow occurring at the medium temperatures varies from type A+B to B+C or C as the testing temperature increases. The average serration amplitude of these Al-containing alloys is larger than that of CoCrFeNiMn alloy due to the enhanced pinning effect. The early small strain produces low-density of dislocation arrays and bowed dislocations in fcc grains while the dislocation climb and shearing mechanism dominate inside bcc grains. The cross-slip and kinks of dislocations are frequently observed and high-density-tangled dislocations lead to dislocation cells after plastic deformation with a high strain.

**Key words:** high-entropy alloys; microstructure; tensile properties; dislocation; serrated flow

## 1 Introduction

High-entropy alloys (HEAs) have been an attractive subject since they are defined as important members of solid solution alloys [1]. HEAs containing five or more principal metallic elements with equimolar or near-equimolar ratio tend to form simple crystal structures instead of intermetallic or amorphous phases. Furthermore, HEAs usually possess excellent mechanical properties especially high resistance against fatigue, corrosion and high-temperature softening [2–11], which make them potential candidates in many industrial applications. The CoCrFeMnNi alloy with a single face-centered cubic (fcc) solid solution phase was much concerned owing to its

thermodynamic stability and good mechanical performance [12]. CANTOR et al [13] just showed the structures and OTTO et al [14] only reported the mechanical properties of this type of single-phase alloy. It has been found that a transition occurred in the deformation mechanism from planar-slip dislocation activity at room temperature to nano twins at cryogenic temperature, and thus an excellent combination between high strength and good ductility is granted for this alloy [3,14].

To further improve the mechanical properties of CoCrFeMnNi alloy without sacrificing its primary characters, a strengthening approach via introducing second phases or precipitates into this base alloy has been explored [15–20]. It has been demonstrated that Al is one of the most effective elements. For instance, the microstructures and

**Foundation item:** Project (11572306) supported by the National Natural Science Foundation of China; Project (WK2090050040) supported by the Fundamental Research Funds for Central Universities, China

**Corresponding author:** Liang-ming PENG; Tel: +86-551-63606964; Fax: +86-551-63606459; E-mail: penglm@ustc.edu.cn  
DOI: 10.1016/S1003-6326(20)65250-5

tensile properties of  $(\text{FeCoNiCrMn})_{100-x}\text{Al}_x$  alloys changed obviously with increasing Al content [15]. Our recent studies examined the creep deformation and dynamic tensile behavior of the thermo-mechanically treated dual-phase  $\text{Al}_x\text{CrMnFeCoNi}$  HEAs [21,22]. Nevertheless, further work is still needed to reveal their mechanical properties and microstructural changes at elevated temperature. On the other hand, it is well-known that the plastic deformation in the conventional alloys and HEAs is mainly attributed to the dislocation motion (slip and/or climb) and deformation twins. Traditional alloys are frequently reported to deform via a jerky way or sudden stress drops which is defined as serrated flow behavior and generally related to dynamic strain aging (DSA) and Portevin-Le Chatellier (PLC) effect [23–26]. However, multi-component HEAs are quite different from the conventional dilute-solute alloys, which lose the traditional sense of ‘solvent’ and ‘solute’, but possess severely distorted lattice attributed to the disordered atomic arrangement. In addition, short-range order (SRO) or short-range clustering (SRC) in HEAs is likely to take effect in its interaction with dislocations. Unfortunately, until date, only a few investigations have been focused on the serration behavior of  $\text{CoCrFeNiMn}$  HEA without Al addition [27,28] and the effects of Al addition remain unknown.

Accordingly, the aim of the present work was to examine the tensile properties of dual-phase  $\text{Al}_x\text{CrMnFeCoNi}$  HEAs ( $x=0.4, 0.5, 0.6, \text{at.}\%$ ) in a wide temperature range. The effects of thermomechanical treatment, Al content and temperature on microstructural evolution, tensile properties and serrated flow behavior were studied systematically.

## 2 Experimental

The cast ingots with nominal compositions of  $\text{Al}_x\text{CrMnFeCoNi}$  ( $x=0, 0.4, 0.5, 0.6, \text{at.}\%$  and subsequently denoted as  $\text{Al}_x$ ) were prepared by vacuum-induction melting a mixture of pure metals ( $\sim 99.9 \text{ wt.}\%$  in purity) in a water-cooled copper crucible. The melting and drop casting were operated in high-purity argon atmosphere to prevent volatilization and oxidation of the constituent elements. To ensure chemical homogeneity, all ingots were melted at least five times. The melted

alloys were drop-cast into a steel mold and the obtained bulk ingots were homogenized at  $1100 \text{ }^\circ\text{C}$  for 24 h in an argon atmosphere. To prevent the plate ingots from cracking under cold rolling condition and severe oxidation at elevated temperature (above  $1000 \text{ }^\circ\text{C}$  for these alloys), the ingots were rolled at  $900 \text{ }^\circ\text{C}$  using a multi-pass route with a reduction in thickness of 0.25 mm at each pass and the final thickness was approximately 5.4 mm with a thickness reduction of 40%. The rolled plates were eventually recrystallized at  $1100 \text{ }^\circ\text{C}$  for 3 h in vacuum, and dog-bone shaped specimens were cut with a wire electrical discharge machine. The tensile samples were tested on the CSS-3905 multi-functional testing machine at both room temperature and elevated temperatures with a strain rate of  $3 \times 10^{-4} \text{ s}^{-1}$ .

The crystal structures of the samples were identified by X-ray diffraction (XRD) (PANalytical X'Pert Pro) with  $\text{Cu K}_\alpha$  radiation and the scanning angle ( $2\theta$ ) ranged from  $20^\circ$  to  $80^\circ$  with a scanning rate of  $5 \text{ }^\circ/\text{min}$ . The alloy specimens were polished using SiC papers to obtain a smooth surface and etched in a solution of hydrogen peroxide and hydrochloric acid. The microstructural observations were conducted on an optical microscope (OM, AxioImager.Alm). The thin foils for transmission electron microscope (TEM, JEF2100F) were mechanically ground to  $55 \mu\text{m}$  approximately and then electro-chemical twin-jet polished in a solution of perchloric acid and ethanol with a volume ratio of 1:15 using an applied voltage of 45 V at  $-30 \text{ }^\circ\text{C}$ . An ImageJ software was employed to estimate the volume fractions of bcc phase and grain size based on calculating at least three individual pictures.

## 3 Results and discussion

### 3.1 XRD diffraction analysis and microstructures

Figure 1(a) shows the XRD patterns of  $\text{Al}_x$  HEAs in as-cast, homogenized and recrystallized states, respectively. Overall, there is almost no apparent difference in phase constituent among the three states for each alloy. The  $\text{Al}_{0.4}$  alloy is composed of almost a simple fcc solid solution whereas both the  $\text{Al}_{0.5}$  and  $\text{Al}_{0.6}$  alloys exhibit fcc+bcc phases. Furthermore, the intensity of bcc-peak increases with increasing Al content,

indicating that the volume fraction of bcc phase in  $Al_{0.6}$  is higher than that in  $Al_{0.5}$ . As evident from Fig. 1(b) for the recrystallized state, the (111) peak shifts to a lower  $2\theta$  angle with increasing Al content due to an increasing lattice distortion.

Figure 2 shows the optical microstructures of as-cast, homogenized and recrystallized  $Al_x$  HEAs. All the cast alloys exhibit dendrite and interdendrite microstructures (Figs. 2(a, d, g)), where the bcc phases (gray areas) distinctly distribute along

the dendrite/interdendrite interface. After the homogenization and subsequent thermomechanical processing, the morphologies are evolved into equiaxed grains consisting of fcc (bright) and bcc (dark) phases (Figs. 2(b, c, e, f, h, i)), respectively. The volume fractions of bcc phase and fcc grain size are estimated as approximately 2%, 13% and 31%, and 90, 35 and 20  $\mu m$  for  $Al_{0.4}$ ,  $Al_{0.5}$  and  $Al_{0.6}$ , respectively. It can be observed that the bcc phases tend to distribute at fcc grain boundaries in the

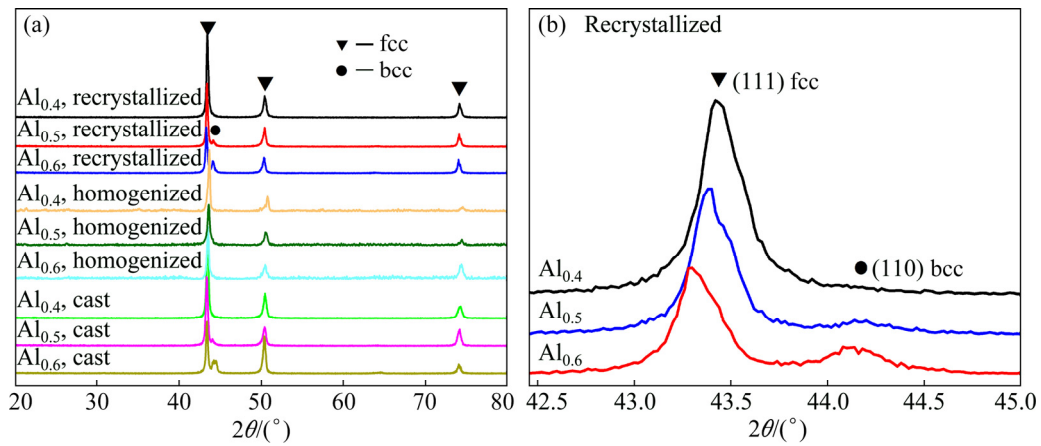


Fig. 1 XRD patterns of  $Al_x$  HEAs (a) and partially enlarged patterns of (111) fcc and (110) bcc peaks (b)

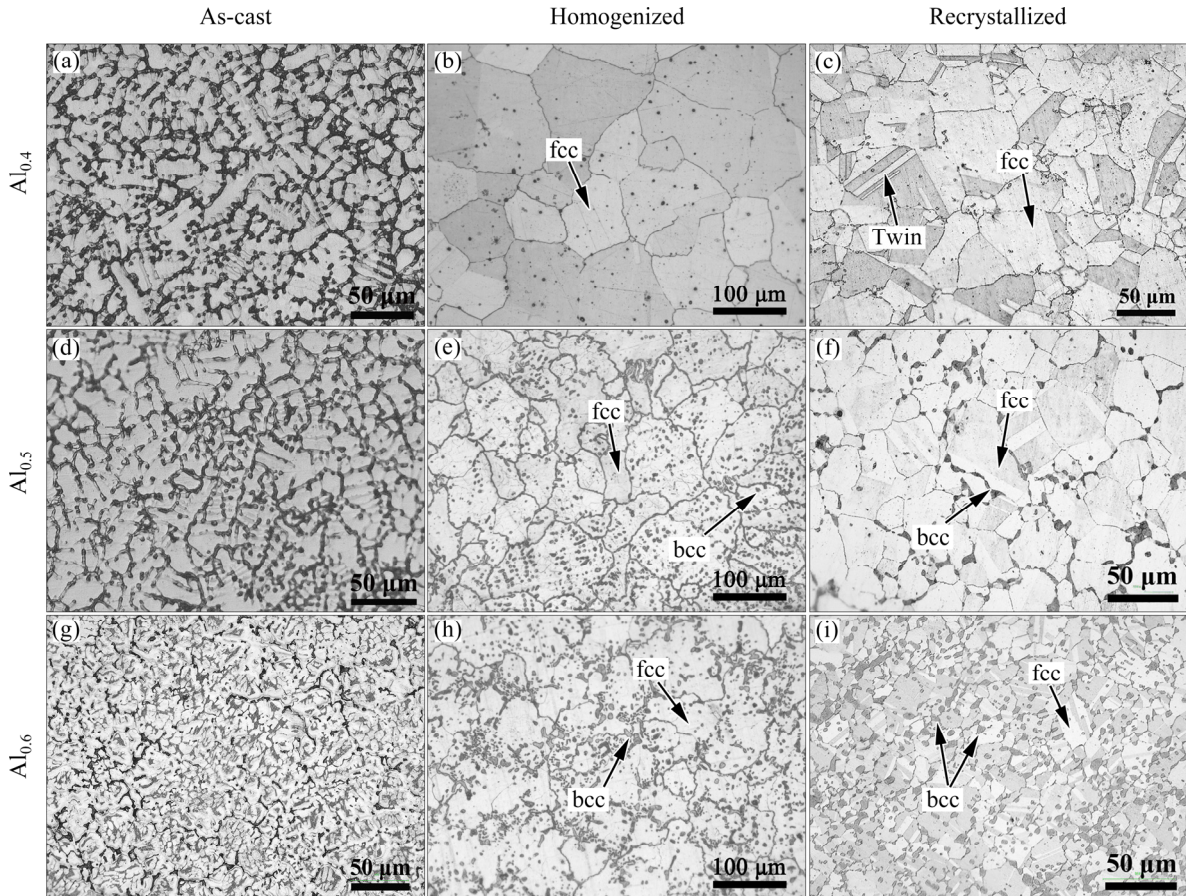


Fig. 2 Optical microstructures of  $Al_x$  HEAs in as-cast, homogenized and recrystallized states

rolled-recrystallized  $\text{Al}_{0.5}$  alloy whereas they are formed both at fcc grain boundaries and inside fcc grains. It is obvious that  $\text{Al}_{0.6}$  alloy possesses significantly refined fcc phases as more bcc phases are nucleated along the fcc boundaries. In addition, several annealing twins are observed inside some fcc grains after thermomechanical processing.

### 3.2 Mechanical properties

The engineering stress–strain curves of the three  $\text{Al}_x$  HEAs are shown in Fig. 3(a), which exhibit typical strength–ductility trade-off rules. The increasing strength of alloys is ascribed to multi-contributions from solid solution, grain-boundary and secondary phase hardening [22]. Figures 3(b, c, d) show the engineering stress–strain curves tested at different temperatures. In general, both the 0.2% offset yield strength,  $\sigma_{0.2}$ , and ultimate tensile strength,  $\sigma_b$ , decrease (Figs. 4(a, b)) with increasing temperature. The temperature dependence of yield strength might be attributed to the thermally induced change in dislocation width which makes an effect of temperature on the Peierls

stress [29]. In contrast, the uniform elongation to fracture,  $\varepsilon_f$ , shows much more complicated temperature dependence. Particularly, the elongation of  $\text{Al}_{0.4}$  and  $\text{Al}_{0.5}$  changes slightly in a plateau-like mode below 500 °C, but drops drastically at 600 °C. However, the elongation for  $\text{Al}_{0.6}$  monotonously decreases until 600 °C. For all alloys, the strain softening dominates after short hardening process at 700 °C.

In order to demonstrate the effects of temperature and Al content on work hardening, as evident from Fig. 3, the engineering stress–strain ( $\sigma$  vs  $\varepsilon$ ) curves were converted to true stress–strain ( $\sigma_T$  vs  $\varepsilon_T$ ) curves using the relationship of  $\sigma_T = \sigma(1 + \varepsilon)$  and  $\varepsilon_T = \ln(1 + \varepsilon)$  (not shown here). According to the acknowledged Considere's criterion [14], high ductility is generally ascribed to high work hardening capability, which is usually described using the work hardening exponent  $n$ , given by the Holloman equation [30]:

$$\sigma_T = k\varepsilon_T^n \quad (1)$$

where  $\sigma_T$  is the true stress,  $\varepsilon_T$  is the true strain

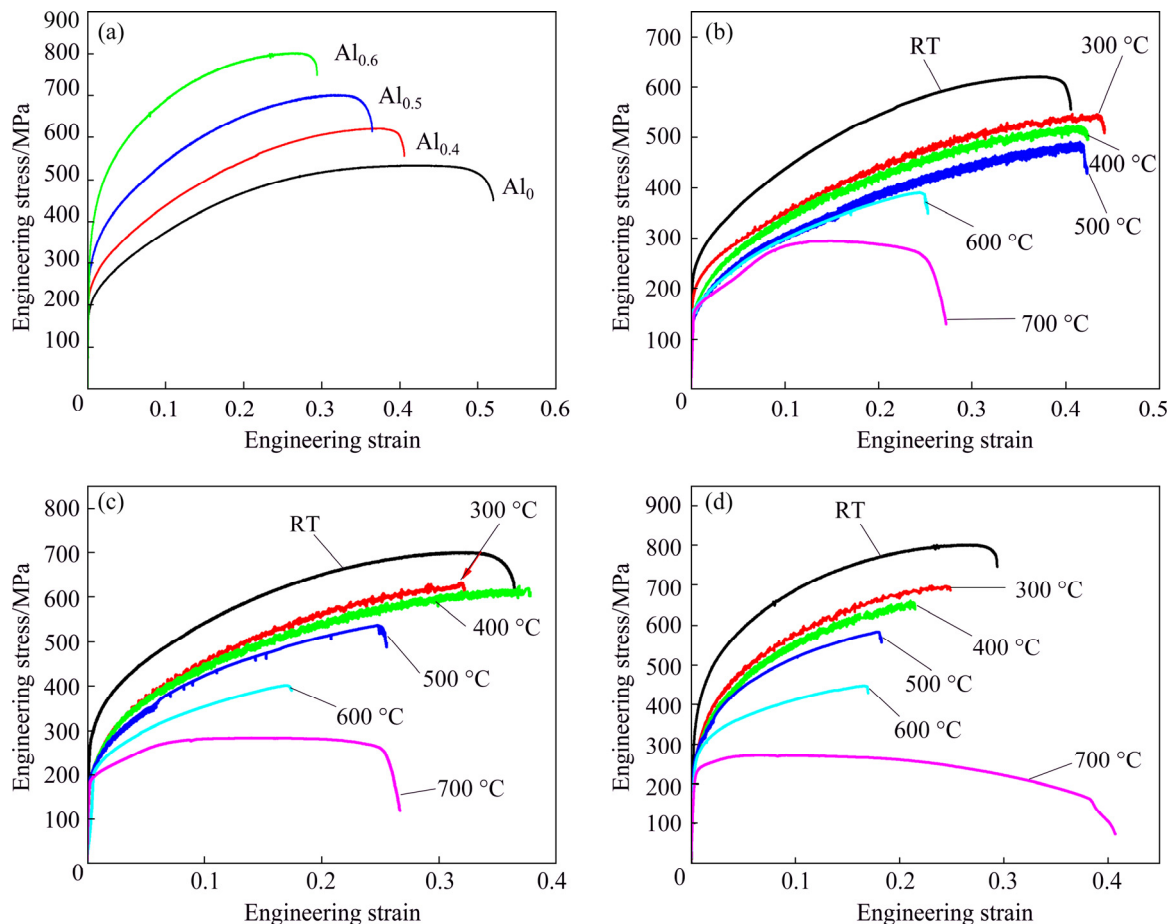


**Fig. 3** Engineering stress–strain curves of specimens for  $\text{Al}_x$  alloys at room temperature (a), and  $\text{Al}_{0.4}$  (b),  $\text{Al}_{0.5}$  (c) and  $\text{Al}_{0.6}$  (d) at elevated temperatures

and  $k$  is the material constant. Thus, the work hardening exponent,  $n$ , can be obtained via evaluating the slope of a plot of  $\ln \sigma_T$  versus  $\ln \varepsilon_c$  at a given temperature and the results are shown in Fig. 4(d). It can be found that the  $n$  value decreases with increasing content of bcc phase.

### 3.3 Serrated flow behavior

As evident from the partially enlarged segments of engineering stress–strain curves in Fig. 5, pronounced serrated flow behaviors even extending from the yield points occur in the three HEAs. The serrated flow is usually classified into A, B and C types based on existing theories and models. In general, type A serration starts with stress increment as the pinning process during which the solutes gather around dislocations and make them motionless. However, the dislocations can break away from these solutes when local stress exceeds a certain limit, inducing a sudden stress drop during the unpinning process [31]. Type B serration appears at higher temperature as the solute atoms diffuse faster than in type A, and therefore it

is much easier for solutes to form more effective pinning. As a result, the serrations are continuous and larger in type B. On the contrary, type C serrations begin with unpinning process, and discontinuous serrations occur relying on the fact that dislocations can move with solutes without getting free from these pinning atoms as temperature increases further [24].

For the present alloys, the evolutions in serration types exhibit obvious dependence on Al content and testing temperature. The  $\text{Al}_{0.4}$  alloy takes the order of type A+B→B→B+C→C at 300–600 °C (Fig. 5(a)). The serrations of  $\text{Al}_{0.5}$  evolve in the path of type A+B at 300 °C → B at 400 °C → B+C at 500 °C. However, the change of type A+B→B→C is observed in  $\text{Al}_{0.6}$  within the identical temperature range as  $\text{Al}_{0.5}$ . In addition,  $\text{Al}_{0.4}$  and  $\text{Al}_{0.6}$  HEAs exhibit interrupted or intermittent type C serrations at higher temperatures (i.e., 600 and 500 °C, respectively).

To obtain deeper insight into the PLC effect, the critical strain as characteristic parameter represents the serration origin where first pinning or

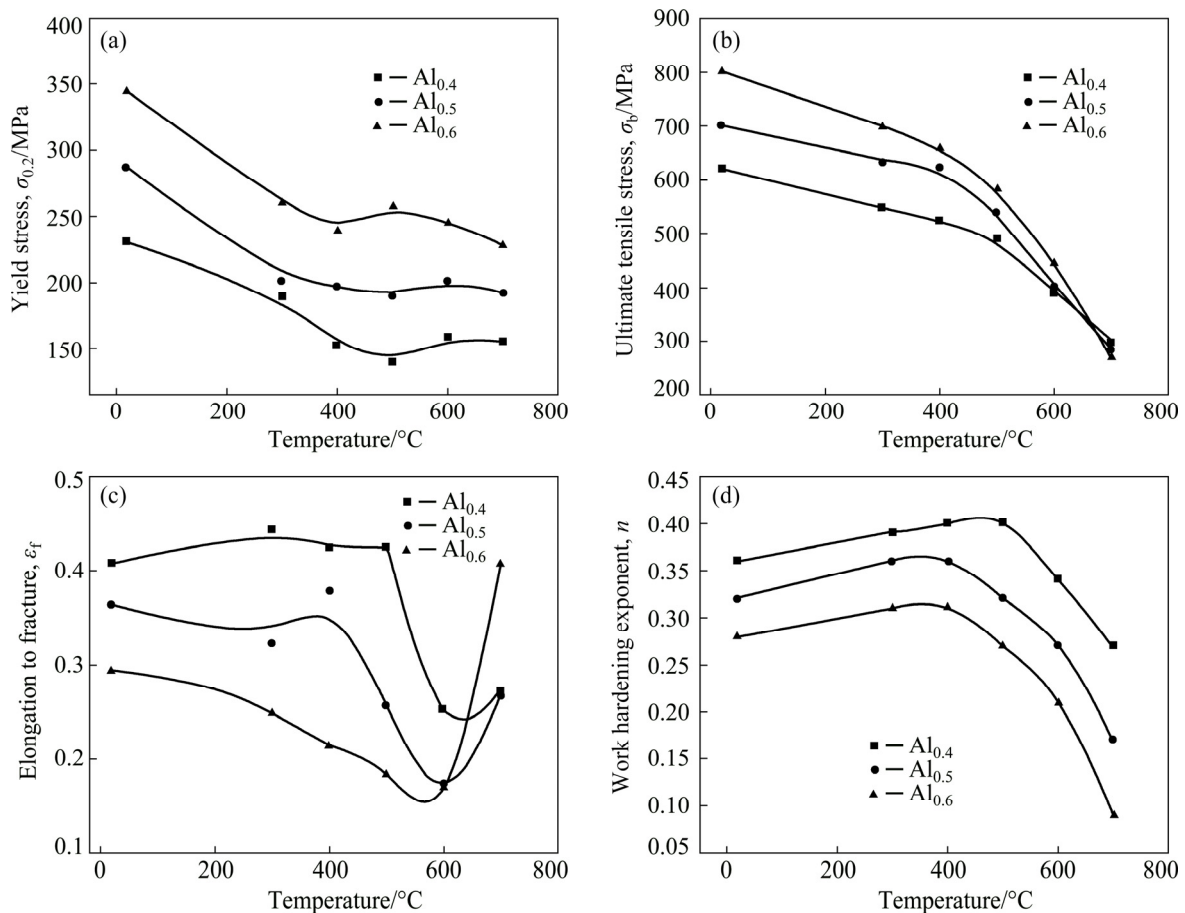


**Fig. 4** Temperature dependence of yield strength,  $\sigma_{0.2}$  (a), ultimate tensile strength,  $\sigma_b$  (b), elongation to fracture,  $\varepsilon_f$  (c) and work hardening exponent,  $n$  (d) for  $\text{Al}_x$  HEAs

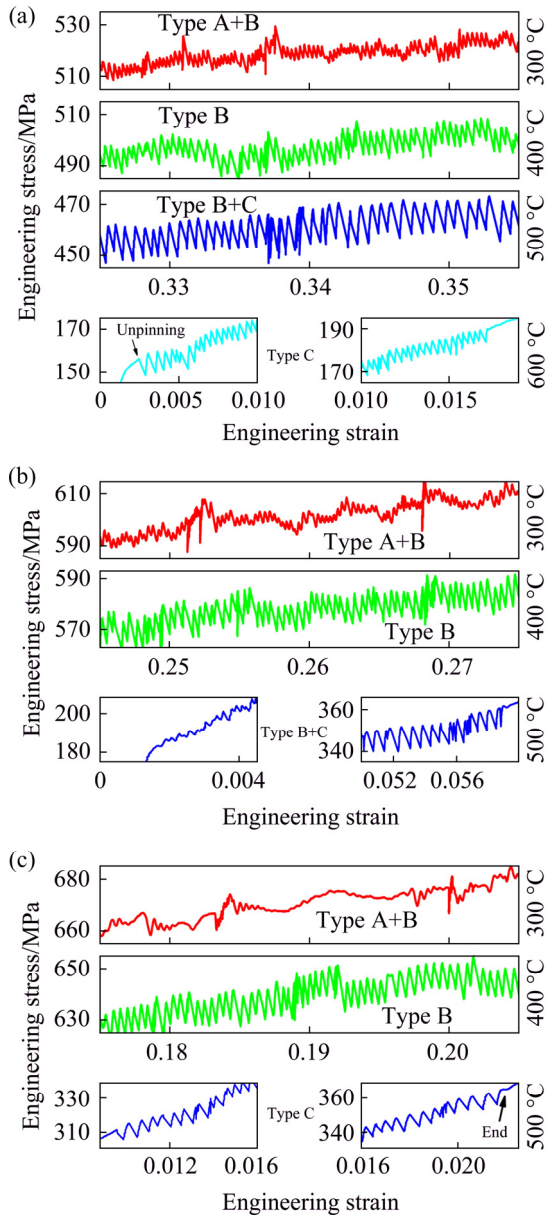


**Fig. 5** Typically enlarged portion of stress–strain curves with serration types for Al<sub>0.4</sub> (a), Al<sub>0.5</sub> (b) and Al<sub>0.6</sub> (c)

unpinning occurs. In this work, the critical strain first decreases and then increases with temperature (Fig. 5), indicating a change from the normal to inverse PLC effect. Generally, abundant time at low strain rate or increased diffusion effect can contribute to earlier pinning for types A and B at low temperature regime, leading to a trend of decreasing critical strain [32]. However, at high temperature, the critical strain in the range of inverse PLC increases linearly with increasing temperature [33].

The serration amplitude as another characteristic parameter is defined as the stress drop

from the peak stress to the bottom stress. It is obvious that the serration amplitude increases firstly and then gradually reaches a saturated value as strain increases (Fig. 6). In general, for a given alloy and except type C, the serration amplitude increases with temperature and plastic deformation strain. The type B+C serration in Al<sub>0.4</sub> at 500 °C exhibits the highest average amplitude of 9.22 MPa. Compared to CoCrFeNiMn alloy [27], the Al-containing alloys show larger serration amplitude

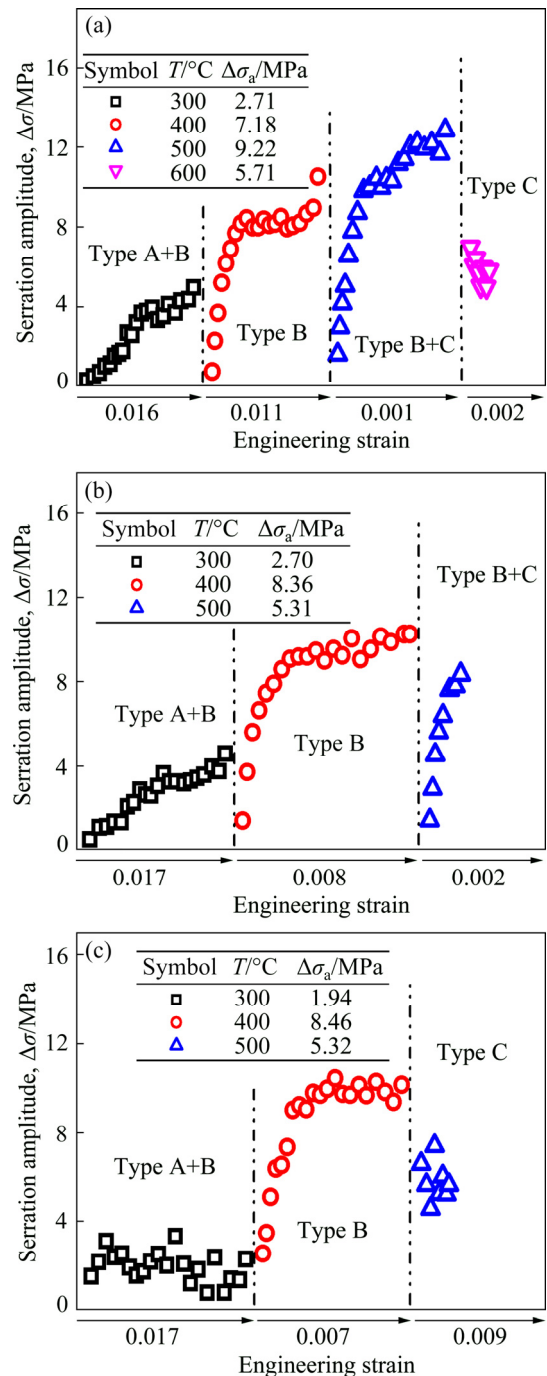


**Fig. 6** Variations of average serration amplitude for Al<sub>0.4</sub> (a), Al<sub>0.5</sub> (b) and Al<sub>0.6</sub> (c) at different temperatures

under the same condition. Substitutional Al atoms can produce larger obstacles in the distorted crystal structure (the atomic radii:  $R_{\text{Al}}=1.4317 \text{ \AA}$ ,  $R_{\text{Cr}}=1.2491 \text{ \AA}$ ,  $R_{\text{Mn}}=1.3500 \text{ \AA}$ ,  $R_{\text{Fe}}=1.2412 \text{ \AA}$ ,  $R_{\text{Co}}=1.2510 \text{ \AA}$ , and  $R_{\text{Ni}}=1.2459 \text{ \AA}$  [34]). As a result, the interactions between solutes and dislocations are effectively intensified to yield larger serration amplitudes, which is consistent with previous results [35]. In addition, as Al content increases, the upper limit temperature for serrated flow decreases, which might result from the stronger pinning effects caused by the increased Al atoms and bcc phase particles. Similar phenomenon was observed in Ni-based superalloys, where the obstacle to dislocation motion was enhanced with additional precipitates and thus the dynamic strain aging (DSA) temperature range was lowered [24]. However, it is worth noting that different from the conventional substitutional solute-containing alloys, there are no dominant matrix elements in the present equiatomic HEAs and it is possible for all the constituent elements to involve in the formation of solute atmosphere around the sliding dislocations. Under such a circumstance, it is difficult to conclude which element is the sole contributing solute atom.

### 3.4 Dislocation substructures and fractography

The dislocation substructures of  $\text{Al}_{0.4}$  and  $\text{Al}_{0.6}$  alloys undergoing plastic strains of 1.2% and 20% at 400 °C are shown in Figs. 7 and 8, respectively. In the early stage of plastic deformation, only low-density dislocations are produced in the two alloys. Short parallel dislocation arrays are observed in  $\text{Al}_{0.4}$  alloy (Fig. 7(a)), and dilute dislocations are bowed inside fcc grains of  $\text{Al}_{0.6}$  alloy (Fig. 7(b)). These dislocations form extended pile-ups at interphase and annealing twinning boundaries. Substructural examination on the deformed CoCrFeMnNi HEA demonstrated that the planar glide of  $1/2\langle 110 \rangle$  dislocations on  $\{111\}$  planes dominates in the early stages of plastic deformation [14]. Moreover, the strong localization of dislocation motion on a limited plane is probably related to the presence of short-range clustering (SRC) or short-range order (SRO) of solute atoms in HEA system. However, typical dislocation jogs formed inside bcc grains imply that plastic deformation is governed by dislocation climb. Simultaneously, coherent nano-precipitates

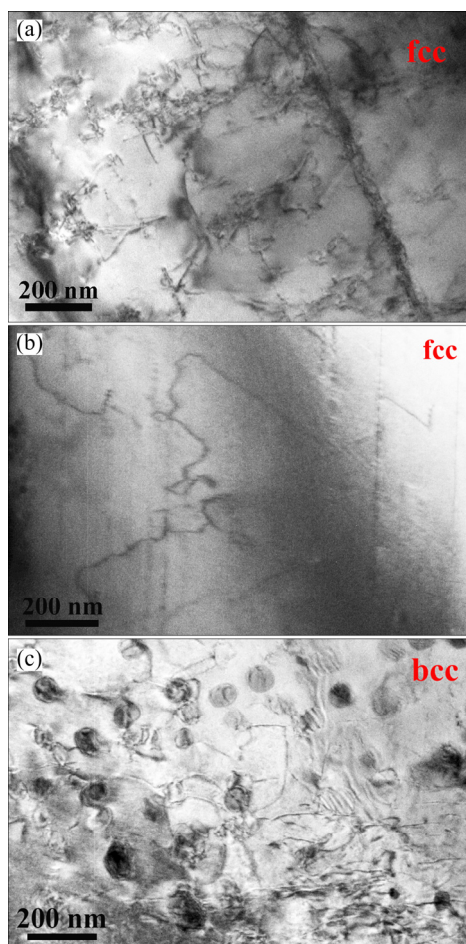


**Fig. 7** Dislocation substructures of  $\text{Al}_{0.4}$  (a) and  $\text{Al}_{0.6}$  (b, c) undergoing plastic strain of 1.2% at 400 °C

are frequently sheared by moving dislocations (Fig. 7(c)), suggesting the control of shearing mechanism. The crystal structure of nano-precipitate is identified as body-centered cubic with a lattice parameter of  $2.8968 \text{ \AA}$  (very close to that of bcc matrix). These A2 bcc nano-precipitates contain abundant Al and Cr [22] and are generated via spinodal decomposition from the initial bcc phase [36]. It is well-known that the low stacking fault energy (SFE) favors the formation of deformation twinings and planar slip while the climbing of dislocations is closely associated with high SFE. Compared to fcc phase, the bcc phase has a higher SFE due to the enriched Al atoms and intrinsic crystal structure [16]. Moreover, the SFE can also increase with temperature, and hence, planar slip vanishes and dislocations tend to climb inside bcc grains at elevated temperature.

After being subjected to high deformation strain, high-density dislocations are produced in the

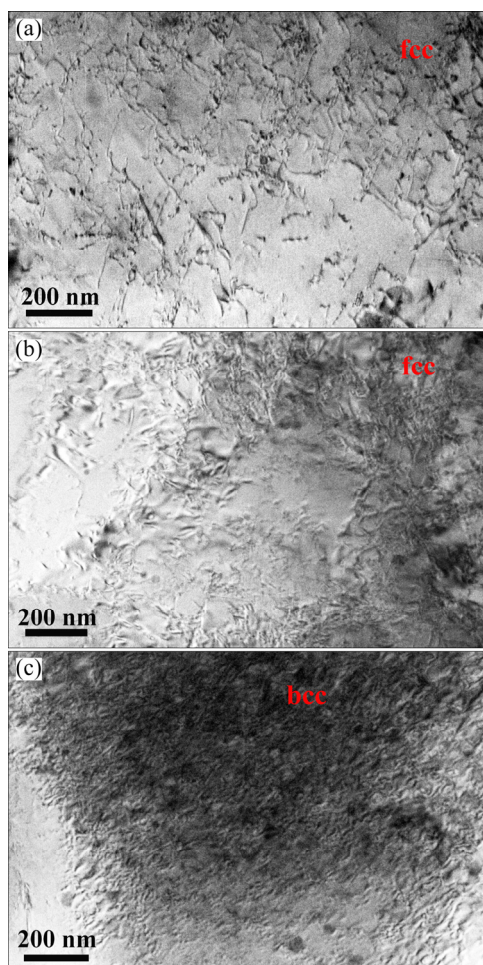


**Fig. 8** Dislocation substructures of  $\text{Al}_{0.4}$  (a) and  $\text{Al}_{0.6}$  (b, c) undergoing plastic strain of 20% at 400 °C

two alloys (Fig. 8). The cross-slip and kinking of dislocations are clearly visible. More fresh slip planes are activated to accommodate the externally imposed strain to make dislocation spread out more uniformly. The formation of kinking and bowing of dislocations via the pinning effect of solute atoms provides the evidence of the serrated flows at intermediate temperature. Besides, dislocation cell structures are formed due to the tangled dislocation networks. Dense dislocations are found to be localized within fcc and bcc grains. The pile-up of dislocations at grain or interphase boundaries can generate a long-range back stress as the obstacle to dislocation motion.

Figure 9 shows typical SEM fractographs of HEAs tested at ambient and elevated temperatures. On the whole, the fracture surfaces are characterized by equiaxed dimples, indicating a typical ductile-fracture mode. Moreover, a micro-

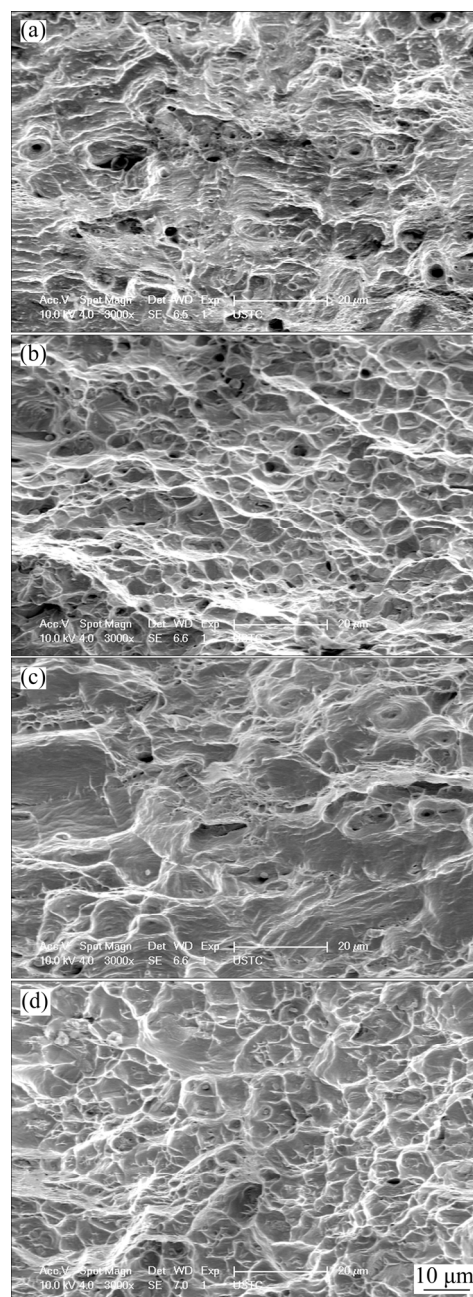


**Fig. 9** SEM micrographs of fracture surfaces for  $\text{Al}_{0.4}$  (a) and  $\text{Al}_{0.6}$  (b) at RT, and  $\text{Al}_{0.4}$  (c) and  $\text{Al}_{0.6}$  (d) at 600 °C

structural dependence of fracture morphology is revealed. For instance, the dimples become smaller and shallower in high Al-containing alloys (Figs. 9(b, d)) as homogeneously distributed bcc grains and high density of boundaries provide more crack sources. As a result, the resistance against deformation instability and work hardening capacity decreases. Therefore,  $\text{Al}_{0.6}$  alloy exhibits lower ductility than  $\text{Al}_{0.4}$  and  $\text{Al}_{0.5}$  alloy under identical testing conditions.

## 4 Conclusions

(1) The cast dendrite of  $Al_xCrMnFeCoNi$  alloys evolves into equiaxed-grain microstructure after a series of thermomechanical treatments. The increment of yield and tensile strength is ascribed to solid solution, grain-boundary and bcc phase strengthening.

(2) Prominent serrated flow behaviors occur at medium temperature with the serration types depending on testing temperature and Al content.  $Al_xCrMnFeCoNi$  alloys exhibit larger serration amplitudes compared to the corresponding base alloy without Al addition due to the enhanced DSA effect.

(3) Small plastic deformation produces dilute pile-ups and bowing dislocations while severe deformation induces tangled dislocation network, frequent interaction of dislocations and formation of cell structures. The fracture morphologies are tightly associated with the initial microstructures especially the amount of bcc phase in the HEAs.

## References

- [1] YE H J W, CHEN S K, LIN S J, GAN J Y, CHIN T S, SHUN T T, TSAU C H, CHANG S Y. Nanostructured high entropy alloys with multiple principal elements: Novel alloy design concepts and outcomes [J]. *Advanced Engineering Materials*, 2004, 6: 299–303.
- [2] POLETTI M G, FIORE G, GILI F, MANGHERINI D, BATTEZZATI L. Development of a new high entropy alloy for wear resistance:  $FeCoCrNiW_{0.3}$  and  $FeCoCrNiW_{0.3+5at.\%}$  of C [J]. *Materials and Design*, 2017, 115: 247–254.
- [3] TIAN Ye, LU Cong-yang, SHEN Yi-fu, FENG Xiao-mei. Microstructure and corrosion property of  $CrMnFeCoNi$  high entropy alloy coating on Q235 substrate via mechanical alloying method [J]. *Surfaces and Interfaces*, 2019, 15: 135–140.
- [4] TIAN Y Z, SUN S J, LIN H R, ZHANG Z F. Fatigue behavior of  $CoCrFeMnNi$  high-entropy alloy under fully reversed cyclic deformation [J]. *Journal of Materials Science and Technology*, 2019, 35(3): 334–340.
- [5] LAPLANCHE G, BERGLUND S, REINHART C, KOSTKA A, FOX F, GEORGE E P. Phase stability and kinetics of  $\sigma$ -phase precipitation in  $CrMnFeCoNi$  high-entropy alloys [J]. *Acta Materialia*, 2018, 161: 338–351.
- [6] TANG Zhi, YUAN Tao, TSAI C W, YE H J W, LUNDIN C D, LIAW P K. Fatigue behavior of a wrought  $Al_{0.5}CoCrCuFeNi$  two-phase high-entropy alloy [J]. *Acta Materialia*, 2015, 99: 247–258.
- [7] CHENG Hu, XIE Yan-chong, TANG Qun-hua, RAO Cong, DAI Pin-qiang. Microstructure and mechanical properties of  $FeCoCrNiMn$  high-entropy alloy produced by mechanical alloying and vacuum hot pressing sintering [J]. *Transactions of Nonferrous Metals Society of China*, 2018, 28: 1360–1367.
- [8] ZHOU Shang-cheng, ZHANG Peng, XUE Yun-fei, WANG Fu-chi, WANG Lu, CAO Tang-qing, TAN Zhen, CHENG Bao-yuan, WANG Ben-peng. Microstructure evolution of  $Al_{0.6}CoCrFeNi$  high entropy alloy powder prepared by high pressure gas atomization [J]. *Transactions of Nonferrous Metals Society of China*, 2018, 28: 939–945.
- [9] LIU Cong, PENG Wen-yi, JIANG C S, GUO Hong-min, TAO Jun, DENG Xiao-hua, CHEN Zhao-xia. Composition and phase structure dependence of mechanical and magnetic properties for  $AlCoCuFeNi$  high entropy alloys [J]. *Journal of Materials Science and Technology*, 2019, 35: 1175–1183.
- [10] WANG Jian-ying, FANG Jing-hua, YANG Hai-lin, LIU Zhi-lin, LI Rui-di. Mechanical properties and wear resistance of medium entropy  $Fe_{40}Mn_{40}Cr_{10}Co_{10}TiC$  composites [J]. *Transactions of Nonferrous Metals Society of China*, 2019, 29: 1484–1494.
- [11] ZHOU Shang-cheng, ZHANG Peng, XUE Yun-fei, WANG Fu-chi. Microstructure evolution of  $Al_{0.6}CoCrFeNi$  high entropy alloy powder prepared by high pressure gas atomization [J]. *Transactions of Nonferrous Metals Society of China*, 2018, 28: 939–945.
- [12] GLUDOVATZ B, HOHENWARTER A, CATOOR D. A fracture-resistant high-entropy alloy for cryogenic applications [J]. *Science*, 2014, 345: 1153–1158.
- [13] CANTOR B, CHANG I T H, KNIGHT P, VINCENT A J B. Microstructural development in equiatomic multicomponent alloys [J]. *Materials Science and Engineering A*, 2004, 375–377: 213–218.
- [14] OTTO F, DLOUHÝ A, SOMSEN C, BEI H, EGGELER G, GEORGE E P. The influences of temperature and microstructure on the tensile properties of a  $CoCrFeMnNi$  high-entropy alloy [J]. *Acta Materialia*, 2013, 61: 5743–5755.
- [15] HE J Y, LIU W H, WANG H, WU Y, LIU X J, NIEH T G, LU Z P. Effects of Al addition on structural evolution and tensile properties of the  $FeCoNiCrMn$  high-entropy alloy system [J]. *Acta Materialia*, 2014, 62: 105–113.
- [16] KLIMOVA M, STEPANOV N, SHAYSULTANOV D, CHERNICHENKO R, YURCHENKO N, SANIN V, ZHEREBTSOV S. Microstructure and mechanical properties evolution of the Al, C-Containing  $CoCrFeNiMn$ -type high-entropy alloy during cold rolling [J]. *Materials*, 2018, 11, 53. doi: 10.3390/ma11010053.
- [17] GAO N, LU D H, ZHAO Y Y. Strengthening of a  $CrMnFeCoNi$  high-entropy alloy by carbide precipitation [J]. *Journal of Alloys and Compounds*, 2019, 792: 1028–1035.
- [18] STEPANOV N D, YURCHENKO N Yu, TIKHONOVSKY M A. Effect of carbon content and annealing on structure and hardness of the  $CoCrFeNiMn$ -based high entropy alloys [J]. *Journal of Alloys and Compounds*, 2016, 687: 59–71.
- [19] WU Z, PARISH C M, BEI H. Nano-twin mediated plasticity in carbon-containing  $FeNiCoCrMn$  high entropy alloys [J]. *Journal of Alloys and Compounds*, 2015, 647: 815–822.
- [20] JO Y H, JUNG S, CHOI W M. Cryogenic strength improvement by utilizing room-temperature deformation

- twinning in a partially recrystallized VCrMnFeCoNi high-entropy alloy [J]. *Nature Communications*, 2017, 8: 15719.
- [21] CAO C M, XU J, TONG W, HAO Y X, GU P, PENG L M. Creep behaviour and microstructural evolution of  $Al_xCrMnFeCoNi$  high-entropy alloys [J]. *Materials Science and Technology*, 2019, 35: 1283–1290.
- [22] CAO C M, TONG W, BUKHARI S H, XU J, HAO Y X, GU P, HAO H, PENG L M. Dynamic tensile deformation and microstructural evolution of  $Al_xCrMnFeCoNi$  high-entropy alloys [J]. *Materials Science and Engineering A*, 2019, 759: 648–654.
- [23] MAX B, VIGUIER B, ANDRIEU E, CLOUE J M. A Re-examination of the Portevin–Le Chatelier effect in alloy 718 in connection with oxidation-assisted intergranular cracking [J]. *Metallurgical and Materials Transactions A*, 2014, 45: 5431–5441.
- [24] CAI Yu-long, TIAN Cheng-gang, FU Shi-hua, HAN Guo-ming, CUI Chuan-yong, ZHANG Qing-chuan. Influence of  $\gamma'$  precipitates on Portevin–Le Chatelier effect of Ni-based superalloys [J]. *Materials Science and Engineering A*, 2015, 638: 314–321.
- [25] AIT-AMOKHTAR H, FRESSENGEAS C, BOUABDALLAH K. On the effects of the Mg content on the critical strain for the jerky flow of Al–Mg alloys [J]. *Materials Science and Engineering A*, 2015, 631: 209–213.
- [26] SAKTHIVEL T, LAHA K, NANDAGOPAL M, CHANDRAVATHI K S, PARAMESWARAN P, PANNEER S S, MATHEW M D, MANNAN S K. Effect of temperature and strain rate on serrated flow behaviour of Hastelloy X [J]. *Materials Science and Engineering A*, 2012, 534: 580–587.
- [27] FU J X, CAO C M, TONG W, HAO Y X, PENG L M. The tensile properties and serrated flow behavior of a thermomechanically treated CoCrFeNiMn high-entropy alloy [J]. *Materials Science and Engineering A*, 2017, 690: 418–426.
- [28] CARROLL R, LEE C, TSAI C W, YEH J W, ANTONAGLIA J, BRINKMAN B A, LEBLANC M, XIE X, CHEN S, LIAW P K, DAHMEN K A. Experiments and model for serration statistics in low-entropy, medium-entropy, and high-entropy alloys [J]. *Scientific Reports*, 2015, 5: 16997.
- [29] WU Z, BEI H, PHARR G M, GEORGE E P. Temperature dependence of the mechanical properties of equiatomic solid solution alloys with face-centered cubic crystal structures [J]. *Acta Materialia*, 2014, 81: 428–441.
- [30] HOLLomon J H. Tensile deformation [J]. *AIME Trans*, 1945, 12: 1–22.
- [31] WU D, CHEN R S, HAN E H. Serrated flow and tensile properties of a Mg–Gd–Zn alloy [J]. *Materials Science and Engineering A*, 2012, 532: 267–274.
- [32] SHARGHI-MOSHTAGHIN R, ASGARI S. The characteristics of serrated flow in superalloy IN738LC [J]. *Materials Science and Engineering A*, 2008, 486: 376–380.
- [33] FU Shi-hua, CHENG Teng, ZHANG Qing-chuan, HU Qi, CAO Peng-tao. Two mechanisms for the normal and inverse behaviors of the critical strain for the Portevin–Le Chatelier effect [J]. *Acta Materialia*, 2012, 60: 6650–6656.
- [34] ZHANG Yong, ZUO Ting-ting, TANG Zhi, GAO M C, DAHMEN K A, LIAW P K, LU Zhao-ping. Microstructures and properties of high-entropy alloys [J]. *Progress in Materials Science*, 2014, 61: 1–93.
- [35] NIU Si-zhe, KOU Hong-chao, ZHANG Yu, WANG Jun, LI Jin-shan. The characteristics of serration in  $Al_{0.5}CoCrFeNi$  high entropy alloy [J]. *Materials Science and Engineering A*, 2017, 702: 96–103.
- [36] MA Yan, YUAN Fu-ping, YANG Mu-xin. Dynamic shear deformation of a CrCoNi medium-entropy alloy with heterogeneous grain structures [J]. *Acta Materialia*, 2018, 148: 407–418.

## $Al_xCrMnFeCoNi$ 高熵合金的显微结构、拉伸性能及锯齿流变形为

徐 钧, 曹承明, 辜 萍, 彭良明

中国科学技术大学 工程科学学院 近代力学系 中科院材料力学行为与设计重点实验室, 合肥 230027

**摘 要:** 研究双相  $Al_xCrMnFeCoNi$  ( $x=0.4, 0.5, 0.6$ , 摩尔分数, %)高熵合金的显微结构、拉伸力学性能与锯齿流变形为。经热力学处理后合金的显微组织由铸态树枝晶演化为由 fcc 和 bcc 组成的等轴晶。随 Al 含量增加, bcc 相体积分数增大, fcc 晶粒尺寸减小, 合金强度得到显著提高。在中温区间, 随试验温度升高, 锯齿流变类型发生  $A+B \rightarrow B+C(C)$  转变。因 Al 原子对位错的钉扎作用较强, 含 Al 合金的平均锯齿应力振幅明显高于不含 Al 的 CoCrFeNiMn 合金。早期的小变形使 fcc 晶粒产生较低密度位错列和弯曲位错, 而 bcc 晶粒中位错的攀移和剪切机制占主导地位。较大塑性变形后, 位错的交滑移和扭折现象频繁发生, 而高密度的位错缠结形成位错胞结构。

**关键词:** 高熵合金; 显微结构; 拉伸性能; 位错; 锯齿流变

(Edited by Bing YANG)